A Focusing Method for B-Scan GPR Images

Caner Ozdemir, Sevket Demirci, and Enes Yigit
Dept. of Electrical-Electronics Engineering, Mersin University
Çiftlikköy, 33343 Mersin, TURKEY

cozdemir@mersin.edu.tr, sdemirci@mersin.edu.tr, enesyigit81@mersin.edu.tr

***Abstract* - In this paper, we propose a simple, but an effective method to solve the focusing problem in B-scan Ground Penetrating Radar (GPR) images. The formulation of the proposed method is presented. Numerical GPR images for different metal targets are generated by the help of a Physical Optics (PO) simulation code. B-scan images for these targets are generated. The method is applied to these examples and successful focused images are obtained.**

***Keywords* – Inversion, radar imaging, B-scan GPR images.**

I. INTRODUCTION

Ground Penetrating Radar (GPR) is an important remote sensing tool mainly used to detect and image subsurface objects [1-3]. Many GPR researchers across different disciplines have applied miscellaneous algorithms in various fields from mine detection to geophysics [4-7]. A usual GPR system collects reflectivity of the ground and beneath objects when the radar is moving on top of the ground. A typical GPR image yields the information of the spatial position and the reflectivity of a buried object. For the monostatic arrangement, a single point scatterer appears as a hyperbola in the space-time GPR image when the radar moves along a synthetic aperture. Such an image construct is sometimes sufficient if the goal is just to detect a pipe or similar objects. However, size, depth and electromagnetic (EM) reflectivity information of the buried object are also needed in most of the GPR applications. If this is case; then, the hyperbolic behavior in space-time GPR image should be translated to a focused one that shows the object's true location and size together with its reflectivity. For this purpose, many image focusing algorithms have been adopted recently [8-11]. Fisher [8] applied reverse-time migration algorithm for GPR profiles. Capineri [9] employed a Hough transformation technique to the B-scan data to obtain better resolved images of pipes in. Leuschen [10] and Morrow [11] implemented back-propagation techniques based on finite difference time-domain (FDTD) reverse-time migration algorithms to solve the focusing problem in B-scan GPR images. Although all these techniques show fair success in getting a better resolved GPR image, computational burden due to iterative work is significant.

In this paper, we propose a computationally simple and fast technique to focus the B-scan space-time GPR images that usually consist of several hyperbolic lines. The details of our method are presented in section II. In the next section, we apply our focusing algorithm to the numerically generated GPR data obtained for various buried objects such as plates, pipes and mine-like objects. The focused images for all these objects are generated accordingly. In the last section, the work is summarized, and issues regarding the effectiveness and the limitations of the proposed method are discussed.

II. THE FOCUSING METHOD

For GPR problems, the radar collects the scattered or back-scattered EM signal from subsurface objects together with many cluttering effects caused mainly by air-to-ground interface and inhomogeneities in the ground. The phase of the received signal is proportional to the trip distance that the EM wave possesses for homogenous mediums. Therefore; for the monostatic configurations, the back scattered signal from a single point-scatterer experiences different round-trip distances as the radar moves along a straight path. For each spatial point, the frequency diversity of the back-scattered signal can be used to get one-dimensional (1-D) range-profile by taking the inverse Fourier Transform (IFT) of the frequency-diverse data. Putting all range profiles side by side produces a 2-D B-scan GPR image in the spatial-depth domain. For a single point-scatterer, it is obvious that the GPR image contains a parabolic hyperbola due to different trip distances as the radar scans the ground. The real object is; in fact, located on the top point of this hyperbola. A typical space-depth B-scan GPR image is shown in Fig.1a. We propose the following methodology to transform the hyperbolic GPR images to the focused ones that should only contain concentrated image patterns. Our transformation method can be summarized as follows: (i) We first get the 2-D B-scan GPR image as described above. For a point scatterer located at (r_o, z_o), the parabolic hyperbola in a GPR image is characterized by the following equation when the radar is moving on a synthetic aperture along Z.

$$r = \sqrt{r_o^2 + (Z - z_o)^2} \qquad (1)$$

Here; Z represent the synthetic aperture vector and r gives the depth of the hyperbola. Assuming that a B-scan GPR image is obtained by the summation of finite number of hyperbolas that corresponds to different points on the object(s) below the ground, we can resolve these points in the following manner. (ii) For each pixel point; (r_i, z_i) in the 2-D original B-scan GPR image; we find the corresponding hyperbolic template using (1) and trace the pixels under this template. (iii) We record the image data for the pixels under this template. At this point, we have a 1-D data; E_p whose length; N is the same as the total number of sampling points in Z. (iv) Then, we take the root-mean-square (*rms*) value of the total energy contained in this 1-D complex data as follows:

$$\{rms\ @(r_i,\ z_i)\} = \sqrt{(|E_p|^2 \cdot |E_p^*|^2)/N} = \frac{1}{\sqrt{N}} \sum |E_p|^2 \qquad (2)$$

Here, the summation runs over the elements of vector $|E_p|^2$. (v) The calculated *rms* value is recorded in the new GPR image at the point (r_i, z_i). This procedure is repeated for all pixels in the original GPR image.

A graphical explanation of the method is demonstrated in Fig. 1 where a 2-D numerically generated B-scan GPR image is shown. This image is generated for an artificial point-scatterer located at (1.6m, 2.5m). Three pixel points in the original image are taken as examples to show their different features while applying our method. Point #1 is located above the true point target. Corresponding hyperbolic curve is plotted in Fig. 1a as a red line. After applying the above procedures, the image data just beneath this curve is plotted in Fig. 1b. It is obvious that the data makes a peak where the curve cuts the real hyperbolic image around z=2.75m. Point #2 is selected at the true object location of (1.6m, 2.5m). The corresponding image data just below the curve matches exactly with the original real hyperbolic image as plotted in Fig. 1c. As the last example, point #3 is selected such that it is situated deeper than the true object location. As obvious from Fig. 1d, there is almost no EM energy exists under the hyperbolic curve corresponding to point #3. Relative *rms* values generated for these 3 points are found to be -12.8dB, 0dB and -34.7 dB, respectively. Therefore; the true image point gives the best *rms* value; while the other points below and the above the true object location gives a much lower *rms* value. The new focused image is obtained by the above method is plotted in Fig. 2. The new focused image clearly pinpoints the true image location at (1.6m, 2.5m). The dynamic range of the display is set to -10dB. The above illustration demonstrates how the method successfully focus the GPR image in real image coordinates.

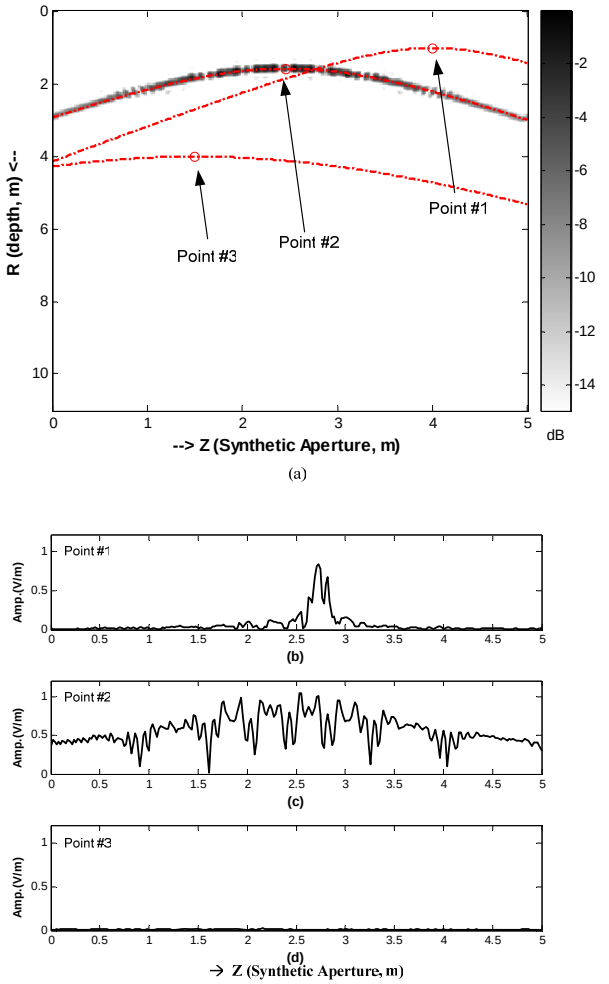

Figure 1. Illustration of the proposed method: (a) Numerically generated B-scan GPR image and the location of the 3 test points and their corresponding hyperbolic templates. The image data under hyperbolic templates for (b) point #1, (c) point #2 and (d) point #3.

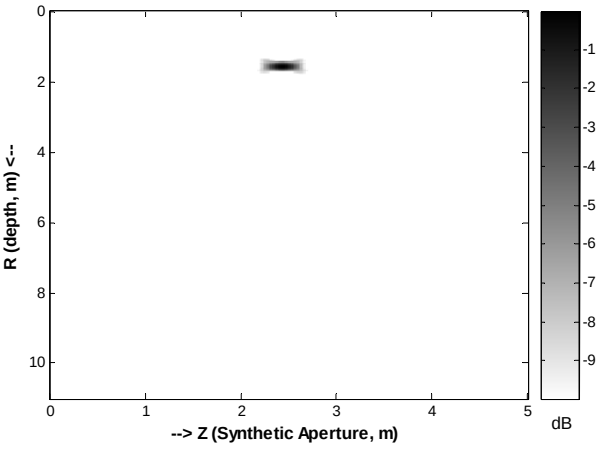

Figure 2. The new, focused GPR image generated by the proposed method.

III. NUMERICAL EXAMPLES

To examine the effectiveness of the method, numerical EM simulation is carried out for various buried objects. For the EM calculation, a physical optics (PO) based simulator that utilizes the shooting and bouncing ray (SBR) technique is used [12]. This simulator can estimate EM scattering from metallic objects only for homogeneous mediums. Therefore; air-ground interface is ignored assuming that the dielectric constant of the ground medium is not too high.

The geometry shown in Fig. 3 is simulated by the help of the above mentioned PO based code. The dielectric constant of the ground is selected as 4.0. The back-scattered EM signature is collected along the synthetic aperture in z-direction ranging from z=0m to z=1m for a total of 64 discrete spatial points. The frequency is also varied from 6.8187 GHz to 9.1443 GHz such that the back-scattered signal is collected for a total of 64 discrete frequencies at each spatial point. Therefore, a 64-by-64, 2-D spatial-frequency B-scan data is obtained for all the examples that we used during this work.

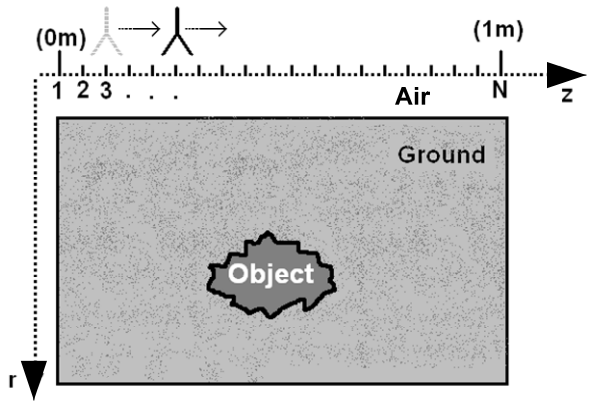

Figure 3. The geometry of the monostatic GPR problem.

The first object that we test with our method is a metal pipe that has a diameter of 6cm and a height of 30cm. The pipe is put 25cm below the surface. The CAD file of the pipe is shown in Fig. 4a. First, we obtain the spatial-depth GPR image as depicted in Fig. 4b. While processing the image, 4-times zero-padding operation is employed to upsample and better resolve the image. Therefore, the image size in all figures is 256-by-256. As expected, the image consists of a thick hyperbola centered at the object's true location. In this figure, the outline of the pipe is drawn in red for referencing purposes. After applying the method explained in Sect. 2, we obtained the new GPR image as shown in Fig. 4c. This image is pretty well focused and better estimates the location of the scattering from top of the pipe. It took only 53 seconds to complete the transformation and form this 256-by-256 new image on an IBM-PC with 1.73 GHz processor and a 1GB of RAM.

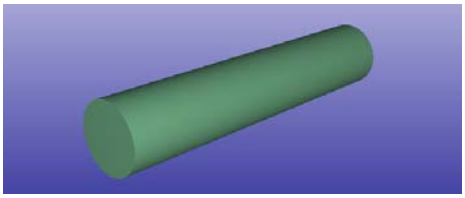

(a)

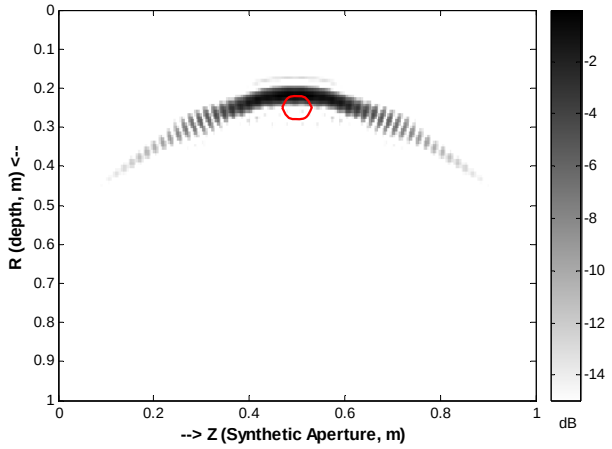

(b)

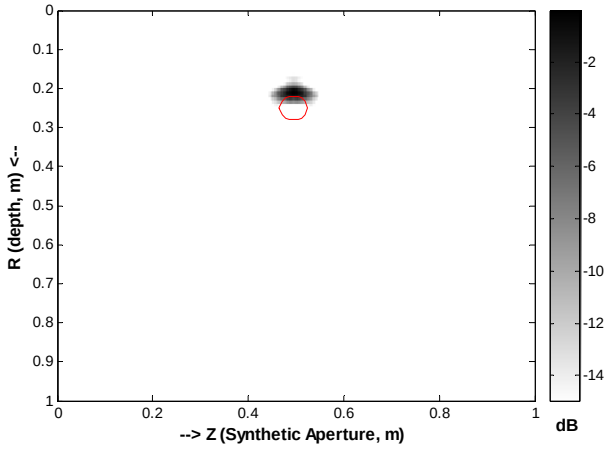

(c)

Figure 4. (a) The CAD file of the pipe (b) Original defocused GPR image (c) Focused GPR image after applying the proposed method.

As a second example, we used three objects (two metal pipes and a metal plate) with different sizes, buried at different locations as the CAD file of these objects is showed in Fig. 5a. The bigger pipe that has a diameter of 12cm and a height of 50cm is put at (r=35cm, z=20cm). The smaller pipe that has a diameter of 6 cm and a height of 30cm is put at (r=25cm, z=50cm). The 10cm-by-10cm metal plate is buried horizontally at (r=30cm, z=75cm). The classical GPR image is obtained in spatial-depth domain by taking the IFT of the 2-D back-scattered data along the frequency

domain as plotted in Fig. 5b. The image is defocused due to reasons that we explained in Sect. 2. The outlines of the objects are again drawn in red. The image obtained by our method in Fig. 5c; however, is well focused to display the key scattering mechanisms from the top of the pipes and the plate. The computation time is again under 1 minute for this example as well. As expected, the image of the scattering from the flat-plate is dominant although it is buried deeper than the pipe at (r=25cm, z=50cm).

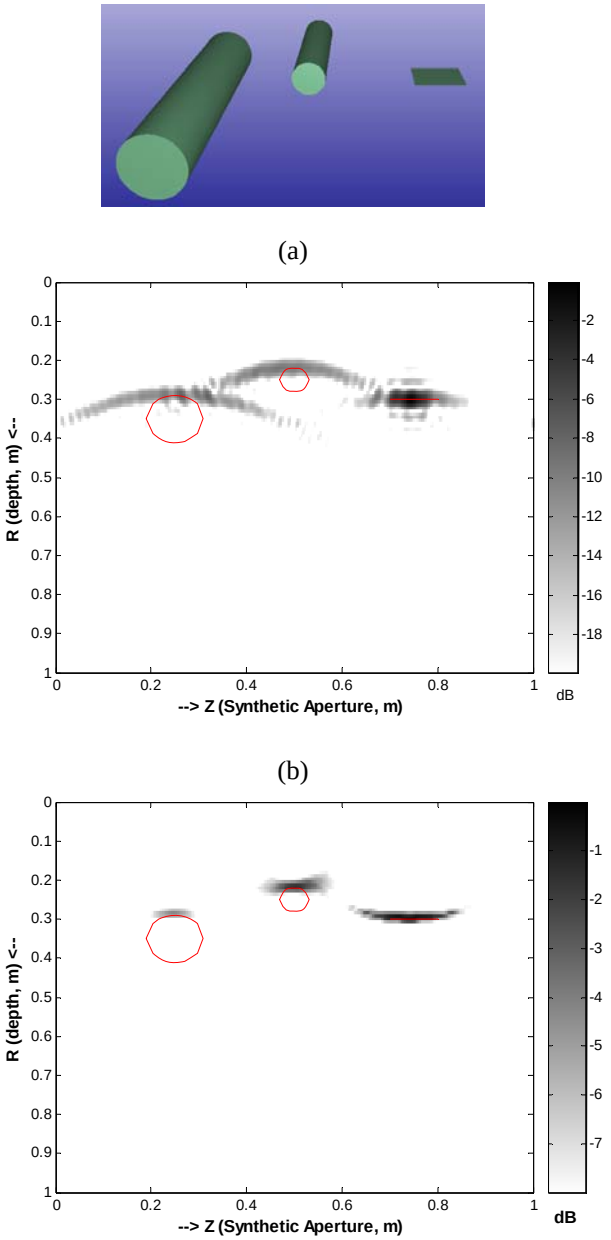

Figure 5. (a) The CAD file of 2-two pipes and a plate (b) Original defocused GPR image (c) Focused GPR image after applying the proposed method.

As the last example, we used two of mine-like, metal objects whose CAD file can be viewed in Fig. 6a. The original GPR image is obtained as seen in Fig. 6b. This image is not as smeared as the pipes since a pipe's circular surface can back-scatter the EM wave at the same level in any direction. However; this is not the case for the objects in this example. We see strong EM energy reflection as the radar passes over the objects. Therefore; the image is not that defocused as in the case of previous examples.

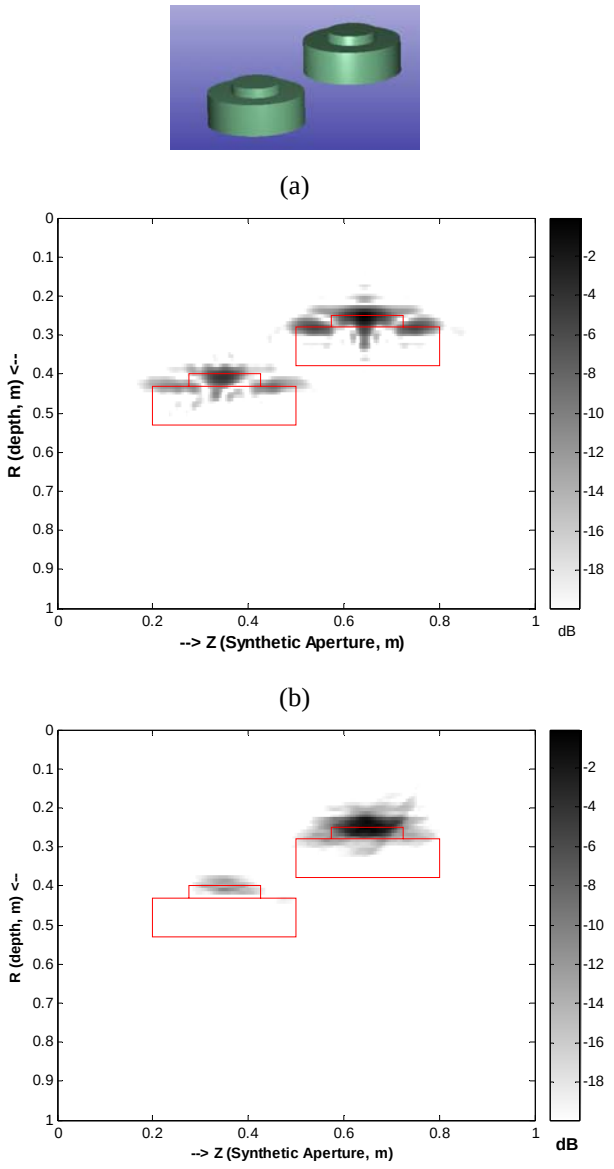

Figure 6. (a) The CAD file of two mine-like objects (b) Original defocused GPR image (c) Focused GPR image after applying the proposed method.

By applying the proposed method, we obtain the new GPR image as shown in Fig. 6c. The simulation time is about the same as previous examples since the image size is the

same. As seen from Fig. 6c., obtained image is more focused and well estimates the dominant scattering especially from the top portion of the objects. However; there are some image feature losses especially for the regions of scattering that fall under the hyperbolic curve corresponding to the dominant scattering points. This situation can be easily seen in this figure. The image strength corresponding to lower object is weaker since its hot spots fall within the hyperbolic curve of the top portion of the upper object.

IV. COMMENTS AND CONCLUSION

In this paper, we introduced a simple, but an effective and fast transformation method to solve the focusing problem in GPR images. The methodology is explained in detail and numerical examples that test the effectiveness of the method are presented. Application of the proposed method to the examples demonstrated that pipes and point scatterer-like objects produce very well focused images in the new GPR image. This is due to the fact that the method uses hyperbolic templates corresponding to point-scatterers and converts these hyperbolas to single image pixels. The plate-like objects in the numerical examples also successfully produced focused images. The algorithm is computationally fast for 2-D B-scan images. This method can also be applied for 3-D B-scan images with a hyperbolic surface template. On the other hand, it is also noticeable that if any scattering mechanism falls under the hyperbolic template of another greater scattering, this point produces a smaller scattering than its original EM energy in the final GPR image. This is the weakness of the proposed method. The last numerical example fairly demonstrates this weakness.

In this work, we could only apply our method to the numerically generated GPR data. During the EM simulation, the medium had to be selected as lossless and homogeneous. However, we wonder the performance of this technique for measured GPR data obtained by real buried targets. As the future work, real GPR data will be examined by the method that we presented in this paper to observe the influence of the air-ground interface, inhomogeneities and the losses in the ground. Furthermore, it will also be very interesting to study dielectric targets with the proposed technique.

ACKNOWLEDGMENTS

This work is supported by the Scientific and Research Council of Turkey (TUBITAK) under project no EEEAG-104E085.

REFERENCES

[1] Daniels, D. J., *Surface-Penetrating Radar*, London: IEE Press (1996).

[2] Peters, L. Jr., Daniels, D. J. and Young, J. D. “Ground penetrating radar as a subsurface environmental sensing tool”, *Proc. IEEE*, vol. 82, no. 12, pp. 1802-1822 (1994).

[3] Vitebskiy, S., Carin, L., Ressler, M.A., and Le, F. H. “Ultrawide-band, short pulse ground-penetrating radar: Simulation and measurement,” *IEEE Trans. Geosci. Remote Sens.*, vol. 35, pp. 762-772 (1997).

[4] Carin, L., Geng, N., McClure, M., Sichina, J. and Nguyen, L. “Ultra-Wide-Band Synthetic- Aperture Radar for Mine-Field Detection,” *IEEE Trans. Antennas Propagat.*, vol. 41, pp. 18-33 (1999).

[5] Halman, J. I., Shubert, K. A. and Ruck, G. T. “SAR processing of ground-penetrating radar data for buried UXO detection: Results from a surface-based system,” *IEEE Trans. Antennas Propagat.*, vol. 46, pp. 1023-1027 (1998).

[6] Sullivan, A., Damarla, R., Geng, N., Dong Y., and Carin, L. “Ultra wide-band synthetic aperture radar for detection of unexploded ordnance: modeling and measurements,” *IEEE Trans. Antennas Propagat.*, vol. 48, pp. 1306–1315 (2000).

[7] Ozdemir, C., Lim, S. and Ling, H. “A synthetic aperture algorithm for ground-penetrating radar imaging,” Microwave *Opt Tech Letters*, vol. 42, pp. 412-414 (2004).

[8] Fisher, E., McMechan, G. A., Annan, A. P., and Cosway, S. W. “Examples of reverse-time migration of single-channel, ground-penetrating radar profiles,” *Geophysics*, vol. 57, pp. 577-586 (1992).

[9] Capineri, L., Grande, P. and Temple, J. A.G. “Advanced image-processing technique for real-time interpretation of ground-penetrating radar images,” *Int. J. Imaging Syst. Tech.*, vol. 9, pp. 51–59 (1998).

[10] Leuschen, C. J., Plumb, R.G. “A matched-filter-based reverse-time migration algorithm for ground-penetrating radar data,” *IEEE Trans. Geosci. Remote Sens.*, vol. 39, pp. 929-936 (2001).

[11] Morrow, I. L., and Van Genderen, P. A. “2D polarimetric backpropagation algorithm for ground-penetrating radar applications,” *Microwave Opt. Technol. Lett.*, vol. 28, pp. 1-4 (2001).

[12] Ling, H., Chou, R., and Lee, S.W. “Shooting and bouncing rays: calculation the RCS of an arbitrary shaped cavity,” *IEEE Trans. Antennas Propagat.*, vol 37, pp. 194-205 (1989).